Large area arrays of discrete single-molecule junctions derived from host-guest complexes

Enrique Escorihuela,[1,2] Jesús del Barrio[1,3], Ross J. Davidson,[4] Andrew Beeby,[4] Paul J. Low,[5] Francesc Prez-Murano,[6] Pilar Cea,[1,2,7,*] Santiago Martin.[1,2,7,*]

[1] *Instituto de Nanociencia y Materiales de Aragón (INMA), CSIC-Universidad de Zaragoza, 50009, Zaragoza, Spain.*
[2] *Departamento de Química Física, Universidad de Zaragoza, 50009, Zaragoza, Spain.*
[3] *Departamento de Química Orgánica, Universidad de Zaragoza, 50009, Zaragoza, Spain.*
[4] *Department of Chemistry, Durham University, South Rd, Durham, DH1 3LE, UK.*
[5] *School of Molecular Sciences, University of Western Australia, 35 Stirling Highway, Crawley, 6009, Western Australia, Australia.*
[6] *Institute of Microelectronics of Barcelona (IMB-CNM, CSIC), 08193, Bellaterra, Spain.*
[7] *Laboratorio de Microscopias Avanzadas (LMA), Universidad de Zaragoza, 50018, Zaragoza, Spain.*

Abstract

The desire to continually reduce the lower limits of semiconductor integrated circuits (IC) fabrication methods continues to inspire interest in unimolecular electronics as a platform technology for the realization of future (opto)electronic devices. However, despite successes in developing methods for the construction and measurement of single-molecule and large-area molecular junctions, exercising control over the precise junction geometry remains a significant challenge. Here, host-guest complexes of the wire-like viologen derivative 1,1′-bis(4-(methylthio)-phenyl)-[4,4′-bipyridine]-1,1′-diium chloride ([**1**][Cl]$_2$) and cucurbit[7]uril (**CB[7]**) have been self-assembled in a regular pattern over a gold substrate. Subsequently, ligandless gold nanoparticles (AuNPs) synthesized *in situ* are deposited over the host-guest array, forming uniform unimolecular junctions. The agreement between the conductance of individual junctions within this array determined by conductive probe atomic force microscope (c-AFM) and true single-molecule measurements for a closely similar host-guest complex within a scanning tunneling microscope break-junction (STM-BJ) indicates the reliable formation of junction-like structures and absence of deleterious intermolecular coupling effects.

1. Introduction

The field of molecular electronics is broadly based on the concept that molecules with appropriately designed chemical structures may perform one (or more) of the basic functions of an electronic circuit element.[1] In this context, electrode | molecule | electrode junctions have proven to be remarkably versatile research tools, providing an opportunity to directly measure the electrical properties of single molecules connected to two macroscopic electrodes under an applied bias. In turn, such data have informed the establishment of the chemical structure-electrical property relationships that underpin the development of future molecular electronic devices.[2-4] However, variations in the electrical response of each individual single-molecule junction that arise from differences and stochastic fluctuations in the molecular conformation, the contact geometry, or the electrode surface geometry within each junction, limit the direct translation of single-molecule junctions from a platform for scientific discovery to a molecular electronic technology.[2, 5, 6]

'Large-area' molecular electronic devices, where molecules are arranged in a parallel fashion within monolayer films, including heterogeneous film structures in which the active molecule is supported within an insulating monolayer provide one solution to the challenges associated with building reproducible and robust junctions.[7-9] These film-based approaches are also more likely compatible with fabrication strategies best suited to incorporation of molecular elements into viable devices.[10, 11] However, whilst film-based large-area junctions may offer advantage in a more uniform molecular geometry, the potential for inter-molecular electronic coupling effects and other intermolecular interactions can affect the properties of the individual molecules and hence the electrical properties of any resulting putative device.[12-15] Therefore, the fabrication of multiple, uniform parallel unimolecular devices, where molecules are localized in defined positions on the surface and at a sufficient distance to avoid potentially deleterious intermolecular coupling effects is a key target for research and development of the new generation of molecular electronic devices. Several strategies have been developed in terms to achieve this goal, including: the use of large 'lily-pad' anchor groups such as the triazatriangulene platform (TATA) which is functionalised by various wire-like or switching motifs and assembled into regular patterns over a gold surface;[16-21] the use of cross-linked metalloporphyrin films to provide a surface template with defined spacing between

surface binding sites for the assembly and growth of wire-like structures;[22-25] and the use of supramolecular host-guest structures to control molecular structure and insulate molecular components.[26-28] Indeed, dynamic processes of supramolecular components arising from external stimuli have been at the heart of some of the most remarkable molecular electronic devices prepared to date, such as Stoddart and Heath's cross-bar molecular memory,[10] inspiring the use of supramolecular components in both single-molecule[29] and large area junctions.[30]

We now report the further use of host-guest complexes as components in molecular electronics, whereby the host provides a degree of control over not only the conformation of, and environment around, the guest molecule, but also allows an ordered spatial distribution of the supramolecular structure (Scheme 1). Moreover, by capping the ordered host-guest film with ligandless gold nanoparticles (AuNPs), an array of single-molecule junctions can be prepared across the surface and characterized by conductive AFM measurements. Therefore, this strategy allows the fabrication of unimolecular junctions neatly distributed in a regular pattern, preserving the advantages of monomolecular devices but arranged in a massively parallel and regular fashion on a surface, while simultaneously avoiding intermolecular electronic coupling effects or other intermolecular interactions that may affect the electrical properties of each junction.

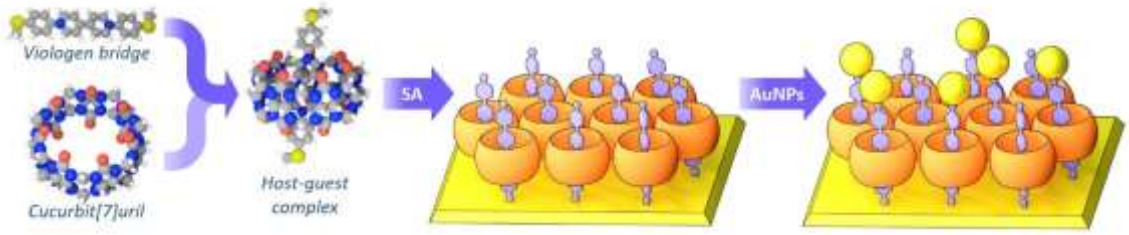

Scheme 1. A schematic showing the strategy used to fabricate multiple, uniform parallel unimolecular devices by assembly of host-guest complexes on a gold surface and the subsequent deposition of ligandless gold nanoparticle top contacts.

2. Results and Discussion

It has been demonstrated elsewhere that the single-molecule conductance of 1,1′-bis(4-(methylthio)-phenyl)-[4,4′-bipyridine]-1,1′-diium chloride ([**1**][Cl]$_2$) increased upon encapsulation within the hydrophobic cavity of cucurbit[8]uril, **CB[8]**.[31] This behavior was interpreted in terms of a two-step (Ulstrup-Kuznetzov) hopping mechanism of charge transport in the 1:1 complex junction, and the reduced outer-sphere reorganization energy

associated with electron transfer arising from the pre-organized viologen backbone of $[\mathbf{1}]^{2+}$ within the **CB[8]** cavity, in line with the expectations of a Marcus-type model. However, analysis of the conductance histograms obtained from STM-BJ measurements also revealed a significant conductance feature associated with 'bimolecular' junctions formed from 1:2 complexes, with two viologens incorporated within the same **CB[8]** cavity. In order to restrict the available space within the cavity and limit the formation of such double-molecule junctions, here attention was turned to the somewhat smaller barrel-shaped host cucurbit[7]uril (**CB[7]**) (Figure 1).

The inclusion of the viologen dication $[\mathbf{1}]^{2+}$ within the **CB[7]** cavity in aqueous solution was assessed by UV-vis spectroscopy.[32] The UV-vis spectrum of **[1]**$[Cl]_2$ displays two intense bands at 264 and 399 nm, which are red-shifted (to 273 and 424 nm, respectively) upon addition of **CB[7]** (Figure 1). This red-shift is attributed to the stabilization of the viologen LUMO upon the formation of the binary **CB[7]**–acceptor complex.[33] This complexation process also induced an increase in the intensity of emission from **[1]**$[Cl]_2$ (Figure S1), in a similar manner to that reported for other **CB[n]** inclusion complexes of viologen derivatives.[34, 35] The formation of a complex of **[1]**$[Cl]_2$ and **CB[7]** was further verified by isothermal titration calorimetry (ITC) experiments (Figure S2 and Table S1).[35]

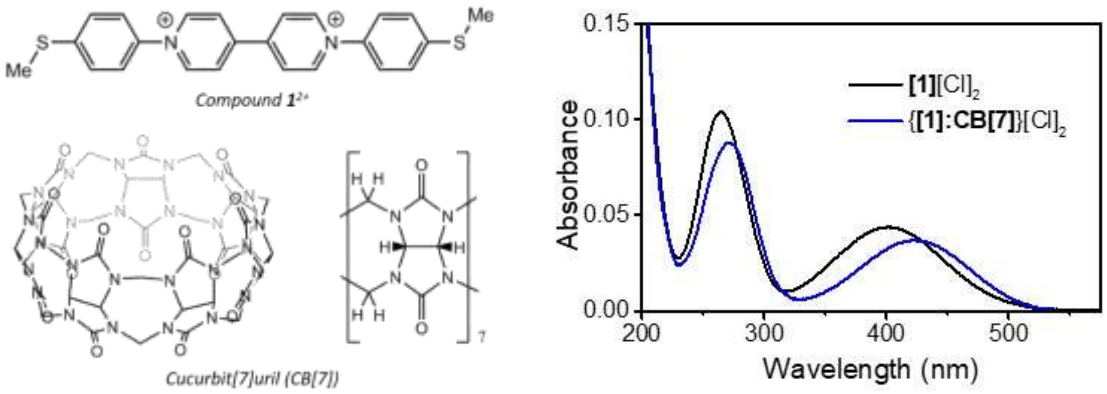

Figure 1. Structures of the guest viologen dication, $[\mathbf{1}]^{2+}$, the host cucurbit[7]uril, **CB[7]**, and UV-vis spectra for a 10^{-6} M aqueous solution of **[1]**Cl_2 and the 1:1 complex {**[1]:CB[7]**}$[Cl]_2$ formed on mixing.

Gold-on-glass, gold-on-mica, or gold-on-quartz crystal microbalance (QCM) substrates were incubated in aqueous solutions of {**[1]:CB[7]**}$[Cl]_2$ to promote formation of self-assembled monolayers, taking advantage of both: (i) the intermolecular

interactions and close packing of the **CB[7]** host that promotes good monolayer film characteristics; and (ii) the thiomethyl anchor group of $[\mathbf{1}]^{2+}$ that chemisorbs to the gold substrate surface.[9, 31, 36-42] The formation of the SAMs was monitored by the change in the QCM resonator frequency (Δf) with time immersed in a {**[1]:CB[7]**}$[Cl]_2$ solution (Figure S3). After ca. 30 hours, no further significant changes in resonator frequency were observed, and a surface coverage could be estimated from fitting the QCM data to the Sauerbrey equation (see SI for further details). Assuming a 1:1 host-guest complex, a surface coverage of $3.7 \cdot 10^{13}$ molecules·cm^{-2} (2.7 nm^2·molecule^{-1}) was obtained. The good agreement between the surface coverage of {**[1]:CB[7]**}$[Cl]_2$ and the estimated surface area occupied by a **CB[7]** molecule given the molecular diameter (ca. 2.0 nm^2·molecule^{-1})[30] indicates the formation of a homogeneous and well-ordered monolayer film of this host-guest complex. Subsequent AFM imaging of the {**[1]:CB[7]**}$[Cl]_2$ SAM supported by a gold-on-mica substrate revealed a uniform monolayer, largely free of perforations or holes, although a small number of aggregates were also evident (Figure 2a). A bearing analysis of the AFM image indicates a surface coverage by the {**[1]:CB[7]**}$[Cl]_2$ SAM of 95 ± 1 % (Figure S4). Additionally, the thickness of the SAM (1.50 ± 0.04) nm, as determined by using the attenuation of the Au4*f* signal in the XPS spectra (Figure S5), and the S…S distance in $[\mathbf{1}]^{2+}$ (ca. 1.95 nm), estimated from Spartan calculations, and the height of **CB[7]** (ca. 0.9 nm), are also consistent with the formation of a monolayer of {**[1]:CB[7]**}$[Cl]_2$ on the gold surface.

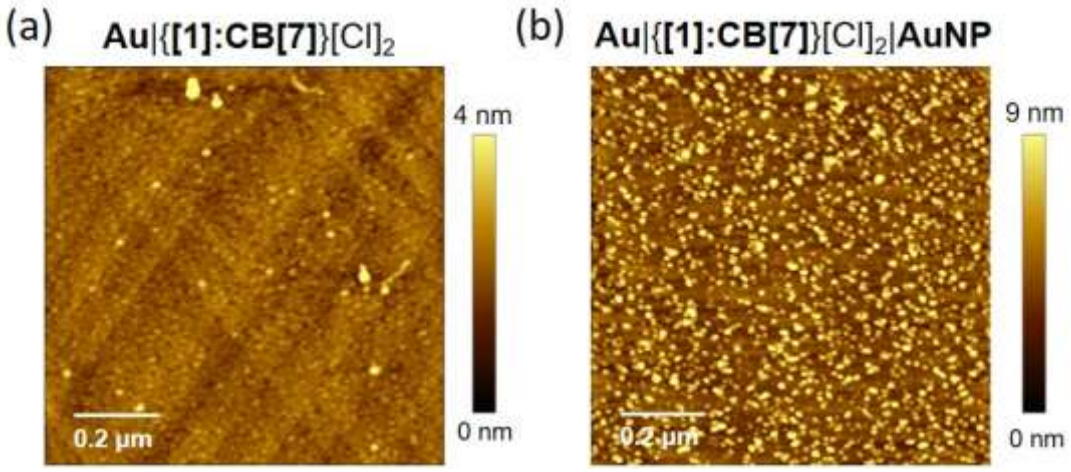

Figure 2. AFM images of (a) a SAM of {**[1]:CB[7]**}$[Cl]_2$ deposited on a gold-on-mica substrate and (b) the same SAM after incubation for 40 minutes in an aqueous dispersion of ligandless AuNPs.

Having established conditions for the formation of well-ordered and tightly packed SAMs of {**[1]:CB[7]**}$[Cl]_2$ on gold, attention was turned to X-ray photoelectron spectroscopy (XPS) to confirm contact between the thiomethyl sulfur anchor and the gold substrate, as well as further evince the 1:1 stoichiometry of the host-guest complex. The XPS data for the S2*p* region from a powder sample of **[1]**Cl_2 displays two peaks, as a consequence of spin–orbit splitting, at 163.3 and 164.5 eV; the peak separation of 1.2 eV and ratio of integrated peak areas of 2:1 being as expected.[43] In contrast, the XPS data from SAMs of {**[1]:CB[7]**}$[Cl]_2$ or a pristine SAM of uncomplexed **[1]**Cl_2 on a gold substrate (see Experimental Section) are more convoluted (Figure 3). For each monolayer, two sets of S2*p* doublet peaks are observed. In each case, a pair of peaks at ca. 163.2 eV and 164.4 eV are observed, at practically the same binding energy as those observed for the powder sample of **[1]**Cl_2, indicating that some of the thioether moieties are free from bonding interactions with the gold substrate. The set of peaks at lower binding energies (161.1 and 162.2 eV) featured in each film are attributed to the thiomethyl sulfur atoms chemisorbed to the gold surfaces.[9, 44] The XPS data for the N1*s* region for powder samples of **CB[7]** contains a peak at 399.9 eV (Figure 3, blue line), attributed to the equivalent nitrogen atoms of the glycoluril units. For **[1]**$[Cl]_2$ a peak at 401.7 eV (Figure 3, red line) is attributed to the positively charged nitrogen atoms of the viologen moiety. Both peaks are observed upon analysis of the SAM of {**[1]:CB[7]**}$[Cl]_2$ with relative integrated areas of 1:14, in perfect agreement with the 1:1 nature of the supramolecular complex observed in solution. The weak peak at 400 eV observed in the **[1]**$[Cl]_2$ powder sample (Figure 3, grey line) is attributed to adventitious nitrogen in the chamber and does not have any relevant implications in the quantification process.

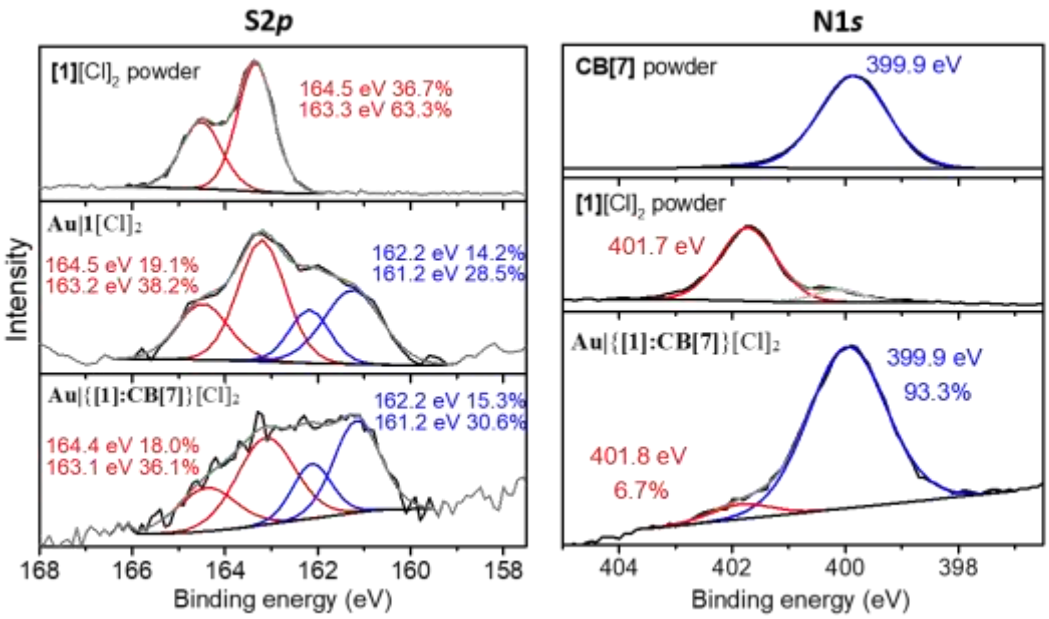

Figure 3. XPS spectra of the S2*p* region for a powder sample of **[1]**$[Cl]_2$, a SAMs of **[1]**$[Cl]_2$ and {**[1]:CB[7]**}$[Cl]_2$ on gold substrates, and also of the N1*s* region of powder samples of **CB[7]** and **[1]**$[Cl]_2$ and a SAM of {**[1]:CB[7]**}$[Cl]_2$ on a gold substrate.

Together, QCM, AFM and XPS data indicate that a 1:1 host-guest complex {**[1]:CB[7]**}[Cl] is readily transferred to a gold substrate through simple self-assembly methods. The high packing density and uniform film surface indicates that this simple in situ assembly and deposition approach represents a good strategy to create arrays of parallel unimolecular devices in which the relative positions of the wire-like guests are controlled by the dimensions of the barrel-shaped host.

To complete each of the individual single-molecular junctions within the film prior to evaluation of their electrical properties, a gold substrate modified by a monolayer of the supramolecular complex, **Au**|{**[1]:CB[7]**}$[Cl]_2$, was prepared and subsequently incubated for a second time in a freshly prepared aqueous dispersion of ligandless gold nanoparticles (AuNPs).[45, 46] The attachment of the AuNPs on the top surface of the film through the exposed thiomethyl anchors was followed by QCM measurements, with a deposition time of 20 min proving to be optimal (Figure S5). Information about the distribution, shape, and size of these top-contacting gold nanoparticles over the Au|{**[1]:CB[7]**}$[Cl]_2$ surface was obtained by AFM imaging (Figure 2b). Analysis of the images reveals that the AuNPs are distributed homogenously on the surface, and well separated from each other although with the presence of certain AuNPs aggregates; a

surface coverage by the AuNPs of ca. 45 ± 1 % is obtained (Figure S7). These surface confined particles present with an average height of 4.1 ± 2 nm and an average diameter (corrected by the tip convolution[47]) of 5.5 ± 2 nm (see SI for further details) as are ligandless nanoparticles. From the relative estimates of surface coverage by the supramolecular complex and the AuNPs, and the average diameter of the AuNPs it can be concluded that some supramolecular complexes within the film are not capped and in other cases between 2 or 3 complexes are contacted by the same AuNP. In contrast, a gold substrate modified by a simple SAM of [**1**][Cl]$_2$, **Au|1**[Cl]$_2$ features a more densely packed array of exposed surface thiomethyl groups and when incubated in the gold nanoparticle solution gave a more complete surface coverage of 92 ± 1 % by the metal particles and a more conventional array of multiple molecule junctions contacted by individual AuNPs (Figure S7).

The electrical properties of the **Au|{[1]:CB[7]}**[Cl]$_2$**|AuNP** structure were determined from *I-V* curves recorded with a conductive atomic force microscope in the peak force tapping mode.[45, 46, 48] In the peak force tapping mode, damage of the surface and detrimental lateral forces are limited as the tip makes intermittent contact with the surface at a frequency of 2 kHz and a low maximum force (peak-force). This soft contact makes PF-TUNA a valuable method for conductivity mapping of delicate samples. The most suitable contact force to record the *I–V* curves demands a compromise between sufficient force to give good electrical contact between the tip and the AuNP without a considerable deformation and yet not a so large force that would result in large deformation of the monolayer underlying the AuNPs and, therefore, in unreasonably high conductance values (Figure 4a).

A range of set-point forces were explored in order to optimize the tip-particle contact. At set points below 2 nN, no significant current through the junction was detected beyond the background noise. For set-point forces between 5 and 20 nN, good electrical contact is obtained between the tip and the particle without deforming considerably the monolayer, permitting conductance values to be extracted from the slope of a linear fit to the Ohmic region of each curve. Higher set-point forces (beyond 20 nN) result in high conductance values, caused by AuNPs being pushed down into the relatively soft underlying monolayer. As the monolayer deforms, the probability of interparticle contacts and contacts between the tip and more than one AuNP also increase, both of which would

also contribute to the higher currents observed. A log–log plot of junction conductance versus the applied set-point force[49] (Fig. 4a inset) shows two distinct power law regimes consistent with this observation: between 5 and 20 nN, the power law exponent is n = 1.75; above 20 nN the exponent n increases to 5.3.

Taking into account these findings, set-point forces above 5 and below 20 nN seem to be optimum to provide an effective electrical contact without significant deformation of the monolayer film. Conductance data was recorded after positioning the PF-TUNA cantilever over an isolated AuNP with a pre-determined 2-3 nm diameter to assure the contact with a unique supramolecular complex according to the surface coverage of 2.7 $nm^2 \cdot molecule^{-1}$ determined by QCM for a 1:1 host-guest complex. The data sets were collected from multiple examples of such junctions, as well using several independently prepared substrates, using set points of 5 and 10 nN. From these data collected by locating the AFM tip across multiple points on the surface and different junctions, average *I-V* curves were constructed (Figure 4b). For completeness, a plot illustrating all the *I–V* curves (ca. 250 curves) recorded, superposed by the average (red lines) at these two set-point forces are shown in Figure S8. A variation of less than half an order of magnitude in the obtained current for all the recorded *I-V* curves (Figure S8) demonstrates the reproducibility, reliability, and low fluctuations of these **Au**|{**[1]:CB[7]**}$[Cl]_2$|**AuNP** structures. This low variation in measurement compares with typical single-molecule measurements, in which current data spanning one or more orders of magnitude are commonly recorded due to the greater dispersion of molecular geometries and contacts within unconstrained junctions.[6, 50-57] Importantly, these curves do not show low resistance traces which are characteristic of metallic short circuits but a linear section at relatively low bias voltages and an increase of the curvature at higher bias; the common behavior observed in metal–molecule–metal junctions. From these average curves, conductance value of $2 \cdot 10^{-5}$ and $6.5 \cdot 10^{-5}$ G_0 (G_0 = 77.5 μS) were obtained for ~~a~~ set-point forces of 5 and 10 nN, respectively. The observed increase of the conductance as the set-point force increases from 5 to 10 nN is attributed to a slight higher deformation of the 1:1 host-guest complex. These values are in good agreement with the single-molecule conductance value determined for the {**[1]:CB[8]**}$[Cl]_2$ host guest complex using the STM break junction (STM-BJ) method ($5.4 \cdot 10^{-5}$ G_0).[31] Additionally, the electrical properties were also determined by positing the tip of the c-AFM directly above the film, without contacting an isolated AuNP (free AuNPs areas in Figure 2b). As shown in Figure

S12, when a similar set-point force is applied when tip of the c-AFM onto an isolated AuNP or directly above the film, practically the same conductance values are obtained, revealing that there is not cross-talk between aligned molecules in both cases and that this conductance is attributed to a single 1:1 host-guest complex.

To demonstrate the role of the supramolecular assembly within the junction on the electrical properties of the devices, the electrical properties for an **Au**|**1**$[Cl]_2$|**AuNP** structure were also determined using the same methodology as indicated above. These more traditional self-assembled molecular 'large area' junctions gave higher conductance values than the supramolecular **Au**|{**[1]:CB[7]**}$[Cl]_2$|**AuNP** junctions when similar set-point forces are applied: $1.8 \cdot 10^{-4}$ or $3.9 \cdot 10^{-4}$ G_0 (Au|**1**$[Cl]_2$|**AuNP)** vs. $2 \cdot 10^{-5}$ or $6.5 \cdot 10^{-5}$ G_0 (**Au**|{**[1]:CB[7]**}$[Cl]_2$|**AuNP**) at 5 nN or 8-10 nN, respectively (Figure 4 and Figure S10). In addition, applying a set-point force of 12 nN to the Au|**1**$[Cl]_2$|**AuNP** junction provokes a considerable increase of the contact both between neighbouring AuNPs and between the AFM tip and these AuNPs as consequence of the high deformation of the monolayer as revealed by the very high conductance value obtained, $2.1 \cdot 10^{-3}$ G_0, where the current recorded saturates at +/- 120 nA limited by the current amplifier employed (Figure 4a and Figure S11). These results imply that for the Au|**1**$[Cl]_2$|**AuNP** structure, multiple $[\mathbf{1}]^{2+}$ structures are contacted by individual AuNPs, in contrast to the SAMs of the 1:1 host-guest complex of cucurbit[7]uril and $[\mathbf{1}]Cl_2$ in which well-ordered arrays of putative single-molecule devices are decorated over the substrate surface with spatial control.

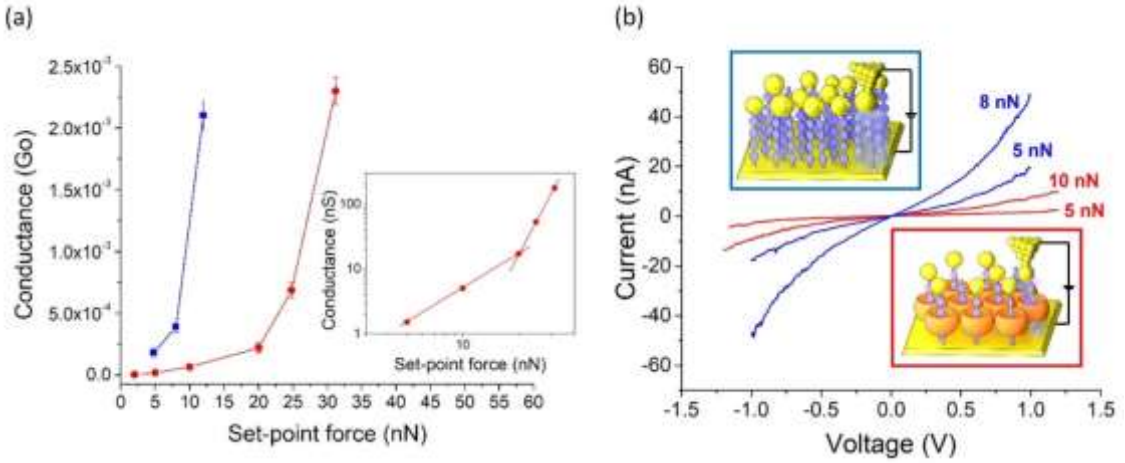

Figure 4. (a) Conductance values determined by locating the tip of the c-AFM onto a gold nanoparticle versus the applied set point-force for an **Au**|{**[1]:CB[7]**}$[Cl]_2$|**AuNP**

structure (red symbols) or **Au**|**1**$[Cl]_2$|**AuNP** structure (blue symbols). Inset: a log–log plot to show of two distinct power regimes in the load force region explored in this work for the **Au**|{**[1]:CB[7]**}$[Cl]_2$|**AuNP** structure. (b) Average *I–V* curves registered when a set-point force of 5, 8 or 10 nN was applied (red lines for the **Au**|{**[1]:CB[7]**}$[Cl]_2$|**AuNP** structure, blue lines for the Au|**1**$[Cl]_2$|**AuNP** structure). Inset: cartoons showing the location of the tip of the c-AFM onto a gold nanoparticle to determine the electrical properties.

3. Conclusions

In conclusion, the 1:1 host-guest complex formed between cucurbit[7]uril and a viologen derivative has been self-assembled on gold substrates to give well-ordered arrays of putative single-molecule devices with excellent spatial control over a large surface area through close packing of the barrel-like host structures (a challenge for the fabrication of a future generation of electronic devices). Given the molecule spacing, appropriately sized ligandless gold nanoparticles (AuNPs) were deposited *in situ* on top of this host-guest arrangement as the top-contact electrode. A variation of less than half an order of magnitude in the current, obtained from the slope of a linear fit to the Ohmic region for all *I-V* curves, demonstrates the reproducibility, reliability, and low fluctuations of the **Au**|{**[1]:CB[7]**}$[Cl]_2$|**AuNP** structure. Additionally, the electrical properties of these unimolecular devices are in agreement to the single molecule conductance determined for this kind of host guest complexes. Future work will be devoted to assessing the suitability of this methodology to other molecular components exhibiting a wider range of electrical functions as well as to other hosts that allow to modulate both the single conductance behavior and shape dependent molecular effects and local volume for electromechanically induce configurational modifications in the guest molecule.

4. Experimental section

General Information. Water was purified on a Milli-Q system (resistivity 18.2 MΩ·cm). The compounds 1,1′-bis(4-(methylthio)-phenyl)-[4,4′-bipyridine]-1,1′-diium chloride (**[1]**$[Cl]_2$)[31] and cucurbit[7]uril (**CB[7]**)[58, 59] were synthesized according to previously published procedures, other reagents were purchased and used as received. All processes and manipulations were carried out under ambient atmosphere and conditions unless otherwise indicated. Gold-on-glass substrates (purchased from Arrandee, Germany) were

flame-annealed at approximately 800-1000 °C with a Bunsen burner to generate Au(111) atomically flat terraces;[60] whilst gold-on-mica substrates (Georg Albert PVD Beschichtungen, Germany) were used as received.

Solution preparation of the host-guest complex, film fabrication and characterization techniques. An aqueous (Milli-Q) solution of the host-guest complex {**[1]:CB[7]**}$[Cl]_2$ (10^{-6} M) was prepared by mixing aqueous solutions ($2 \cdot 10^{-6}$ M) of both components in a 1:1 volume ratio. Self-assembled monolayers (SAMs) of the host-guest complex were subsequently prepared by immersing a gold-on-glass or gold-on-mica substrate in this solution and left undisturbed for 30 hours. After this time, the substrates were carefully removed, rinsed with water and then dried under a N_2 flow. Whilst, SAM of **[1]**$[Cl]_2$ were prepared by immersing a gold-on-glass or gold-on-mica substrate in an aqueous 10^{-6} M solution of this compound for 24 hours.

Isothermal titration calorimetry experiments were carried out using a VP-ITC titration calorimetric system (MicroCal LLC, Northampton, MA). Typically, an aqueous solution of [**1**]$[Cl]_2$ (50 μM) in the calorimetric cell was titrated with an aqueous solution of **CB[7]** (0.90 mM). All solutions were thoroughly degassed and carefully loaded into the cells to avoid bubble formation during stirring. The heat evolved after each injection of ligand was obtained from the integral of the calorimetric signal. The heat associated with the binding reaction was obtained as the difference between the heat of reaction and the corresponding heat of dilution, the latter estimated as a constant heat throughout the experiment and included as an adjustable parameter in the analysis.

UV-visible spectra of solutions were obtained with a Varian Cary 50 Bio UV-vis spectrophotometer in quartz cuvettes with an incident angle of 90°. A Bruker Multimode 8 microscope with a Nanoscope V control unit was used to record the atomic force microscopy (AFM) images under ambient conditions at a scan rate of 1 Hz in the tapping mode using RTESPA-150 AFM probes purchased from Bruker (90-210 kHz resonant frequency, 5 $N \cdot m^{-1}$ spring constant and 8 nm nominal tip radius). X-Ray Photoelectron Spectroscopy (XPS) measurements were obtained with a Kratos AXIS ultra DLD spectrometer with a monochromatic Al Kα X-ray source (1486.6 eV) using a pass energy of 20 eV. The photoelectron take-off angle was 90^o with respect to the sample plane. Binding energies of the samples were referenced to the C1s peak (284.8 eV) to

compensate surface charge effects. Quartz Crystal Microbalance (QCM) measurements were carried out on AT-cut a-quartz crystals (resonant frequency of 5 MHz) patterned with circular gold electrodes on both sides using a Stanford Research Systems microbalance model QCM200. The fluorescence spectra were recorded by means of a Varian Cary Eclipse spectrophotometer in quartz cuvettes of 1 cm.

Gold nanoparticle preparation. Ligandless gold nanoparticles (5.5 ± 2 nm diameter) were prepared *in situ* by adding an aqueous solution of $NaBH_4$ ($1.0 \cdot 10^{-3}$ M, 0.5 mL) to a vigorously stirred aqueous solution of $HAuCl_4$ ($1.0 \cdot 10^{-5}$ M, 30 mL) held at 0 ºC using an ice-water bath.[45] Incubation of the SAM modified gold substrate in the dispersion of AuNPs took place immediately after mixing the reactants with the solution while being stirred at 0 ºC.

Molecular Conductance Measurements. A Bruker ICON microscope in the Peak Force Tunneling AFM (PF-TUNA™) mode with a PF-Tapping™ cantilever tip from Bruker (coated with Pt/Ir 20 nm, ca. 25 nm radius, 0.4 $N \cdot m^{-1}$ spring constant and 70 kHz resonance frequency) was used to perform the conductive-AFM (c-AFM) measurements under conditions of closely controlled humidity (ca. 30%), in an N_2 atmosphere.

Conflicts of interest

There are no conflicts to declare.

Acknowledgements

E.E. gratefully acknowledges the award of a DGA fellowship from the Government of Aragon. P.C. and S.M. are grateful for financial assistance in the framework of the projects PID2019-105881RB-I00, TED2021-131318B-I00, and PID2022-141433OB-I00 funded by MCIN/AEI/10.13039/501100011033 and European Union "NextGenerationEU"/PRTR as well as Gobierno de Aragón through the grant E31_20R with European Social Funds (Construyendo Europa desde Aragón). J.D.B acknowledges grant RYC-2015-18471, funded by MCIN/AEI/10.13039/501100011033 and by "European Social Fund Investing in your future;" and the grant CTQ2017-84087-R supported by MCIN/AEI/10.13039/501100011033, and by "European Regional Development Fund a way of making Europe" by the European Union. R.J.D. and A.B.

gratefully acknowledge the EPSRC grant EP/M029204/1. P.J.L. gratefully acknowledges support for work in the area of molecular electronics from the Australian Research Council Discovery Program (DP190100073, DP190100075 and DP220100790).

References

1. T. A. Su, M. Neupane, M. L. Steigerwald, L. Venkataraman and C. Nuckolls, *Nat. Rev. Mater.*, 2016, **1**.
2. L. Sun, Y. A. Diaz-Fernandez, T. A. Gschneidtner, F. Westerlund, S. Lara-Avila and K. Moth-Poulsen, *Chem. Soc. Rev.*, 2014, **43**, 7378-7411.
3. D. Xiang, X. L. Wang, C. C. Jia, T. Lee and X. F. Guo, *Chem. Rev.*, 2016, **116**, 4318-4440.
4. C. W. Fuller, P. S. Padayatti, H. Abderrahim, L. Adamiak, N. Alagar, N. Ananthapadmanabhan, J. Baek, S. Chinni, C. Choi, K. J. Delaney, R. Dubielzig, J. Frkanec, C. Garcia, C. Gardner, D. Gebhardt, T. Geiser, Z. Gutierrez, D. A. Hall, A. P. Hodges, G. Hou, S. Jain, T. Jones, R. Lobaton, Z. Majzik, A. Marte, P. Mohan, P. Mola II, P. Mudondo, J. Mullinix, T. Nguyen, F. Ollinger, S. Orr, V. Ouyang, P. Pan, N. Park, D. Porras, K. Prabhu, C. Reese, T. Ruel, T. Sauerbrey, J. R. Sawyer, P. Sinha, J. Tu, A. G. Venkatesh, V. S., L. Zheng, S. Jin, J. M. Tour, G. M. Church, P. W. Mola and B. Merriman, *PNAS*, 2022, **119**, 2112812119.
5. H. M. Liu, N. Wang, J. W. Zhao, Y. Guo, X. Yin, F. Y. C. Boey and H. Zhang, *ChemPhysChem*, 2008, **9**, 1416-1424.
6. W. Haiss, S. Martin, E. Leary, H. van Zalinge, S. J. Higgins, L. Bouffier and R. J. Nichols, *J. Phys. Chem. C*, 2009, **113**, 5823-5833.
7. S. Casalini, C. A. Bortolotti, F. Leonardi and F. Biscarini, *Chem. Soc. Rev.*, 2017, **46**, 40-71.
8. L. Herrer, S. Martin, A. Gonzalez-Orive, D. C. Milan, A. Vezzoli, R. J. Nichols, J. L. Serrano and P. Cea, *J. Mater. Chem. C*, 2021, **9**, 2882-2889.
9. E. Escorihuela, P. Cea, S. Bock, D. C. Milan, S. Naghibi, H. M. Osorio, R. J. Nichols, P. J. Low and S. Martin, *J. Mater. Chem. C*, 2020, **8**, 672-682.
10. J. E. Green, J. W. Choi, A. Boukai, Y. Bunimovich, E. Johnston-Halperin, E. DeIonno, Y. Luo, B. A. Sheriff, K. Xu, Y. S. Shin, H. R. Tseng, J. F. Stoddart and J. R. Heath, *Nature*, 2007, **445**, 414-417.
11. A. J. Bergren, L. Zeer-Wanklyn, M. Semple, N. Pekas, B. Szeto and R. L. McCreery, *J. Phys-Condens. Mat.*, 2016, **28**.
12. H. Song, H. Lee and T. Lee, *J. Am. Chem. Soc.*, 2007, **129**, 3806-3807.
13. Y. Dubi, *J. Phys. Chem. C*, 2014, **118**, 21119-21127.
14. K. Slowinski, R. V. Chamberlain, C. J. Miller and M. Majda, *J. Am. Chem. Soc.*, 1997, **119**, 11910-11919.
15. A. Martin-Barreiro, R. Soto, S. Chiodini, A. Garcia-Serrano, S. Martin, L. Herrer, F. Perez-Murano, P. J. Low, J. L. Serrano, S. Marcos, J. Galban and P. Cea, *Adv. Mater. Interfaces*, 2021, **8**, 2100876.
16. H. Jacob, S. Ulrich, U. Jung, S. Lemke, T. Rusch, C. Schutt, F. Petersen, T. Strunskus, O. Magnussen, R. Herges and F. Tuczek, *Phys. Chem. Chem. Phys.*, 2014, **16**, 22643-22650.

17. U. Jung, S. Kuhn, U. Cornelissen, F. Tuczek, T. Strunskus, V. Zaporojtchenko, J. Kubitschke, R. Herges and O. Magnussen, *Langmuir*, 2011, **27**, 5899-5908.
18. S. Kuhn, B. Baisch, U. Jung, T. Johannsen, J. Kubitschke, R. Herges and O. Magnussen, *Phys. Chem. Chem. Phys.*, 2010, **12**, 4481-4487.
19. F. L. Otte, S. Lemke, C. Schutt, N. R. Krekiehn, U. Jung, O. M. Magnussen and R. Herges, *J. Am. Chem. Soc.*, 2014, **136**, 11248-11251.
20. Z. M. Wei, X. T. Wang, A. Borges, M. Santella, T. Li, J. K. Sorensen, M. Vanin, W. P. Hu, Y. Q. Liu, J. Ulstrup, G. C. Solomon, Q. J. Chi, T. Bjornholm, K. Norgaard and B. W. Laursen, *Langmuir*, 2014, **30**, 14868-14876.
21. Q. Wang, L. Ma, Z. H. Liu, X. Zhang, Z. Y. Zhang, Z. C. Shangguan, X. H. Huang, Y. Q. Liu, J. T. Lv, H. M. Zhang, L. F. Chi and T. Li, *Sci. China Mater.*, 2018, **61**, 1345-1350.
22. Q. Ferreira, L. Alcacer and J. Morgado, *Nanotechnology*, 2011, **22**, 435604.
23. Q. Ferreira, A. M. Braganca, L. Alcacer and J. Morgado, *J. Phys. Chem. C*, 2014, **118**, 7229-7234.
24. Z. S. Wang, K. Qian, M. A. Oner, P. S. Deimel, Y. Wang, S. Zhang, X. X. Zhang, V. Gupta, J. Li, H. J. Gao, D. A. Duncan, J. V. Barth, X. Lin, F. Allegretti, S. X. Du and C. A. Palma, *ACS Appl. Nano Mater.*, 2020, **3**, 11752-11759.
25. E. Escorihuela, A. Concellon, I. Marin, V. J. Kumar, L. Herrer, S. A. Moggach, A. Vezzoli, R. J. Nichols, P. J. Low, P. Cea, J. L. Serrano and S. Martin, *Mater. Today Chem.*, 2022, **26**, 101067.
26. D. C. Milan, M. Krempe, A. K. Ismael, L. D. Movsisyan, M. Franz, I. Grace, R. J. Brooke, W. Schwarzacher, S. J. Higgins, H. L. Anderson, C. J. Lambert, R. R. Tykwinski and R. J. Nichols, *Nanoscale*, 2017, **9**, 355-361.
27. Y. Ie, Y. Okamoto, T. Inoue, S. Tone, T. Seo, Y. Honda, S. Tanaka, S. K. Lee, T. Ohto, R. Yamada, H. Tada and Y. Aso, *J. Phys. Chem. Lett.*, 2019, **10**, 3197-3204.
28. L. Herrer, S. Naghibi, I. Marin, J. S. Ward, J. M. Bonastre, S. J. Higgins, S. Martin, A. Vezzoli, R. J. Nichols, J. L. Serrano and P. Cea, *Adv. Mater. Interfaces*, 2023, **10**, 2300133.
29. H. L. Chen and J. F. Stoddart, *Nat. Rev. Mater.*, 2021, **6**, 804-828.
30. C. Q. Yang and H. L. Chen, *ACS Appl. Nano Mater.*, 2022, **5**, 13874−13886
31. W. Zhang, S. Y. Gan, A. Vezzoli, R. J. Davidson, D. C. Milan, K. V. Luzyanin, S. J. Higgins, R. J. Nichols, A. Beeby, P. J. Low, B. Y. Li and L. Niu, *ACS Nano*, 2016, **10**, 5212-5220.
32. H. J. Kim, W. S. Jeon, Y. H. Ko and K. Kim, *PNAS*, 2002, **99**, 5007-5011.
33. F. Biedermann and O. A. Scherman, *J. Phys. Chem. B*, 2012, **116**, 2842-2849.
34. M. Fathalla, N. L. Strutt, J. C. Barnes, C. L. Stern, C. F. Ke and J. F. Stoddart, *Eur. J. Org. Chem.*, 2014, **2014**, 2873-2877.
35. M. Freitag, L. Gundlach, P. Piotrowiak and E. Galoppini, *J. Am. Chem. Soc.*, 2012, **134**, 3358-3366.
36. Y. S. Park, A. C. Whalley, M. Kamenetska, M. L. Steigerwald, M. S. Hybertsen, C. Nuckolls and L. Venkataraman, *J. Am. Chem. Soc.*, 2007, **129**, 15768-15769.
37. E. Leary, A. La Rosa, M. T. Gonzalez, G. Rubio-Bollinger, N. Agrait and N. Martin, *Chem. Soc. Rev.*, 2015, **44**, 920-942.
38. L. Li, J. Z. Low, J. Wilhelm, G. M. Liao, S. Gunasekaran, C. R. Prindle, R. L. Starr, D. Golze, C. Nuckolls, M. L. Steigerwald, F. Evers, L. M. Campos, X. D. Yin and L. Venkataraman, *Nat. Chem.*, 2022, **14**, 1061-1067.
39. X. T. Wang, T. L. R. Bennett, A. Ismael, L. A. Wilkinson, J. Hamill, A. J. P. White, I. M. Grace, O. V. Kolosov, T. Albrecht, B. J. Robinson, N. J. Long, L. F. Cohen and C. J. Lambert, *J. Am. Chem. Soc.*, 2020, **142**, 8555-8560.
40. A. Ismael, X. T. Wang, T. L. R. Bennett, L. A. Wilkinson, B. J. Robinson, N. J. Long, L. F. Cohen and C. J. Lambert, *Chem. Sci.*, 2020, **11**, 6836-6841.
41. L. J. O'Driscoll, X. T. Wang, M. Jay, A. S. Batsanov, H. Sadeghi, C. J. Lambert, B. J. Robinson and M. R. Bryce, *Angew. Chem. Int. Ed.*, 2020, **59**, 882-889.

42. T. L. R. Bennett, M. Alshammari, S. Au-Yong, A. Almutlg, X. T. Wang, L. A. Wilkinson, T. Albrecht, S. P. Jarvis, L. F. Cohen, A. Ismael, C. J. Lambert, B. J. Robinson and N. J. Long, *Chem. Sci.*, 2022, **13**, 5176-5185.
43. H. R. Tseng, S. A. Vignon and J. F. Stoddart, *Angew Chem Int Edit*, 2003, **42**, 1491-1495.
44. F. Sander, J. P. Hermes, M. Mayor, H. Hamoudi and M. Zharnikov, *Phys. Chem. Chem. Phys.*, 2013, **15**, 2836-2846.
45. H. M. Osorio, P. Cea, L. M. Ballesteros, I. Gascon, S. Marques-Gonzalez, R. J. Nichols, F. Perez-Murano, P. J. Low and S. Martin, *J. Mater. Chem. C*, 2014, **2**, 7348-7355.
46. A. Moneo, A. Gonzalez-Orive, S. Bock, M. Fenero, I. L. Herrer, D. C. Milan, M. Lorenzoni, R. J. Nichols, P. Cea, F. Perez-Murano, P. J. Low and S. Martin, *Nanoscale*, 2018, **10**, 14128-14138.
47. J. Canet-Ferrer, E. Coronado, A. Forment-Aliaga and E. Pinilla-Cienfuegos, *Nanotechnology*, 2014, **25**, 395703.
48. L. M. Ballesteros, S. Martin, J. Cortes, S. Marques-Gonzalez, F. Perez-Murano, R. J. Nichols, P. J. Low and P. Cea, *Adv. Mater. Interfaces*, 2014, **1**, 1400128.
49. D. J. Wold and C. D. Frisbie, *J. Am. Chem. Soc.*, 2001, **123**, 5549-5556.
50. R. J. Nichols, W. Haiss, S. J. Higgins, E. Leary, S. Martin and D. Bethell, *Phys. Chem. Chem. Phys.*, 2010, **12**, 2801-2815.
51. S. Martin, W. Haiss, S. J. Higgins and R. J. Nichols, *Nano Lett.*, 2010, **10**, 2019-2023.
52. C. S. Wang, A. S. Batsanov, M. R. Bryce, S. Martin, R. J. Nichols, S. J. Higgins, V. M. Garcia-Suarez and C. J. Lambert, *J. Am. Chem. Soc.*, 2009, **131**, 15647-15654.
53. X. L. Li, J. He, J. Hihath, B. Q. Xu, S. M. Lindsay and N. J. Tao, *J. Am. Chem. Soc.*, 2006, **128**, 2135-2141.
54. F. Chen, X. L. Li, J. Hihath, Z. F. Huang and N. J. Tao, *J. Am. Chem. Soc.*, 2006, **128**, 15874-15881.
55. M. Kamenetska, S. Y. Quek, A. C. Whalley, M. L. Steigerwald, H. J. Choi, S. G. Louie, C. Nuckolls, M. S. Hybertsen, J. B. Neaton and L. Venkataraman, *J. Am. Chem. Soc.*, 2010, **132**, 6817-6821.
56. S. Y. Quek, M. Kamenetska, M. L. Steigerwald, H. J. Choi, S. G. Louie, M. S. Hybertsen, J. B. Neaton and L. Venkataraman, *Nat. Nanotechnol.*, 2009, **4**, 230-234.
57. E. J. Dell, B. Capozzi, K. H. DuBay, T. C. Berkelbach, J. R. Moreno, D. R. Reichman, L. Venkataraman and L. M. Campos, *J. Am. Chem. Soc.*, 2013, **135**, 11724-11727.
58. J. Kim, I. S. Jung, S. Y. Kim, E. Lee, J. K. Kang, S. Sakamoto, K. Yamaguchi and K. Kim, *J. Am. Chem. Soc.*, 2000, **122**, 540-541.
59. A. Day, A. P. Arnold, R. J. Blanch and B. Snushall, *J. Org. Chem.*, 2001, **66**, 8094-8100.
60. W. Haiss, D. Lackey, J. K. Sass and K. H. Besocke, *J. Chem. Phys.*, 1991, **95**, 2193-2196.

Table of Contents (TOC)

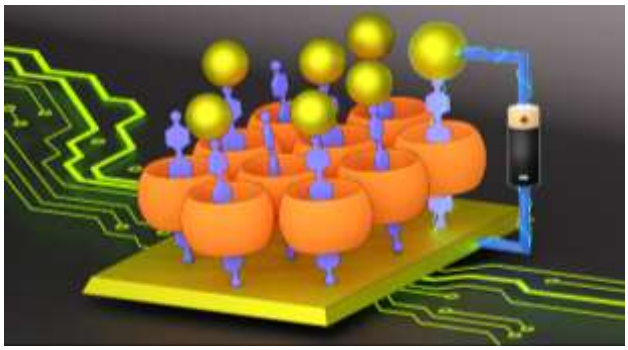

Supporting information

Large area arrays of discrete single-molecule junctions derived from host-guest complexes

Enrique Escorihuela,[1,2] Jesús del Barrio[1,3], Ross J. Davidson,[4] Andrew Beeby,[4] Paul J. Low,[5] Francesc Prez-Murano,[6] Pilar Cea,[1,2,7,*] Santiago Martin.[1,2,7,*]

[1] *Instituto de Nanociencia y Materiales de Aragón (INMA), CSIC-Universidad de Zaragoza, 50009, Zaragoza, Spain.*
[2] *Departamento de Química Física, Universidad de Zaragoza, 50009, Zaragoza, Spain.*
[3] *Departamento de Química Orgánica, Universidad de Zaragoza, 50009, Zaragoza, Spain.*
[4] *Department of Chemistry, Durham University, South Rd, Durham, DH1 3LE, UK.*
[5] *School of Molecular Sciences, University of Western Australia, 35 Stirling Highway, Crawley, 6009, Western Australia, Australia.*
[6] *Institute of Microelectronics of Barcelona (IMB-CNM, CSIC), 08193, Bellaterra, Spain.*
[7] *Laboratorio de Microscopias Avanzadas (LMA), Universidad de Zaragoza, 50018, Zaragoza, Spain.*

S1. Characterization of 1[Cl]$_2$−CB[7] interaction in solution

Fluorescence Spectroscopy

The fluorescent emission of **[1]**[Cl]$_2$ in aqueous solutions demonstrates an enhancement upon the addition of **CB[7];** similar observations have been made concerning p-tolyl-viologen derivatives upon host-guest inclusion.[1-2]

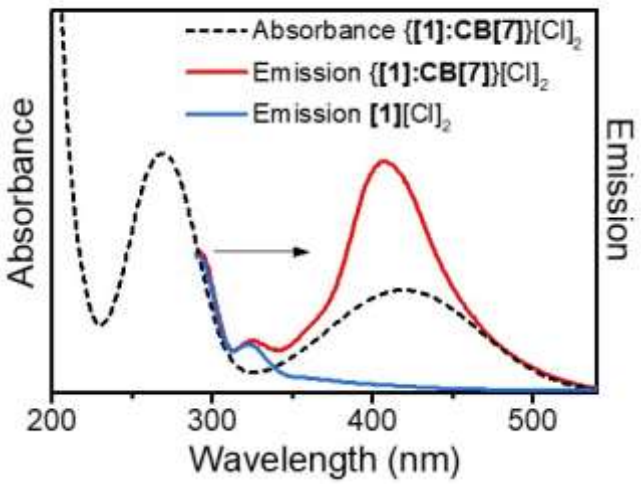

Figure S1. Emission spectra of **[1]**[Cl]$_2$ and {**[1]:CB[7]**}[Cl]$_2$ in 10^{-6} M aqueous solution and absorbance spectrum of {**[1]:CB[7]**}[Cl]$_2$.

The supramolecular assembly of **CB[7]** and **[1]**[Cl]$_2$ was monitored by ITC (Figure S2). The upper plot shows the thermogram (thermal power as a function of time) and the lower panel shows the binding isotherm, *i.e.* **CB[7]**-normalized heat effect per injection as a

function of molar ratio. The equilibrium constants and enthalpies were obtained from the fitting to a cooperative binding model (Table S1).[3] Experiments were carried out in water at 25 °C.

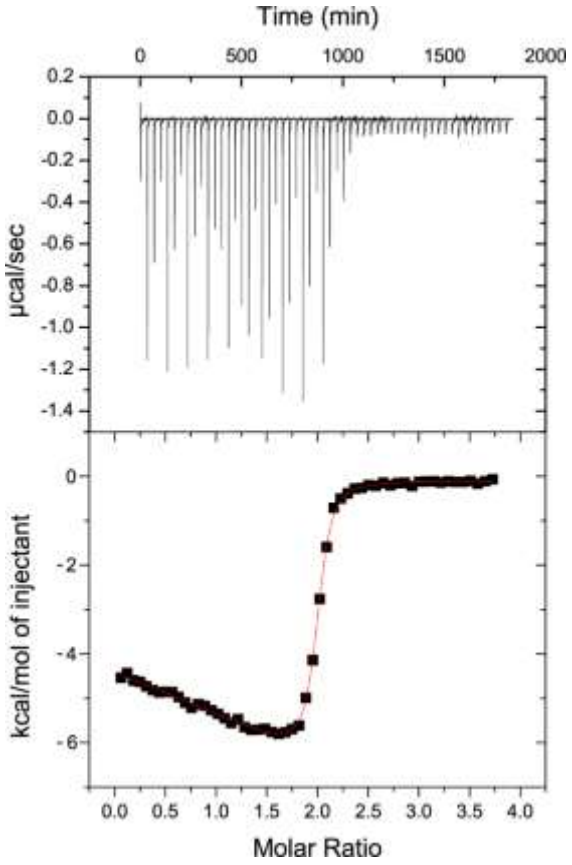

Figure S2. Calorimetric titration for the {**[1]:CB[7]**}$[Cl]_2$ interaction. The titration was carried out in water at 25 °C.

Table 1. Thermodynamic parameters for the interaction between **CB[7]** and **[1]**$[Cl]_2$ as determined by ITC.

Host–Guest Interaction	K_a (10^7) (M^{-1})	α	ΔH (kcal/mol)	Δh (kcal/mol)
1^{2+} + 2CB[7] → $CB[7]_2$:1^{2+}	1.2	0.72	-1.05	-0.4

The titrations were carried out in water at 25 °C. K_a and α are the site-specific association constant and the cooperativity constant respectively. The site-specific binding enthalpy and cooperativity enthalpy are ΔH and Δh respectively. Relative error in the site-specific association constant is 10%.

S2. QCM measurements to determine the surface coverage of a {[1]:CB[7]}$[Cl]_2$ SAM.

To evaluate and follow the formation of a SAM of {**[1]:CB[7]**}$[Cl]_2$, a gold quartz crystal microbalance (QCM) substrate was incubated in a 10^{-6} M solution of {**[1]:CB[7]**}$[Cl]_2$ and the variation in the resonator frequency was monitored with the time (Figure S3). The response of the QCM frequency to a change in mass of the resonator is given by Sauerbrey equation[4] (Eq. 1)

$$\Delta f = -\frac{2 \cdot f_0^{\,2} \cdot \Delta m}{A \cdot \rho_q^{1/2} \cdot \mu_q^{1/2}} \qquad \text{(Eq. 1)}$$

where f_0 is the fundamental resonant frequency of ca. 5 MHz, Δm(g) is the change in mass, A is the area of the electrode, μ_q is the shear modulus (2.95×10^{11} dyn/cm^2), ρ_q is the density of the quartz (2.65 g/cm^3), and the molecular weights of **1** and **CB[7]** are 473.5 and 1162.96 g/mol, respectively.

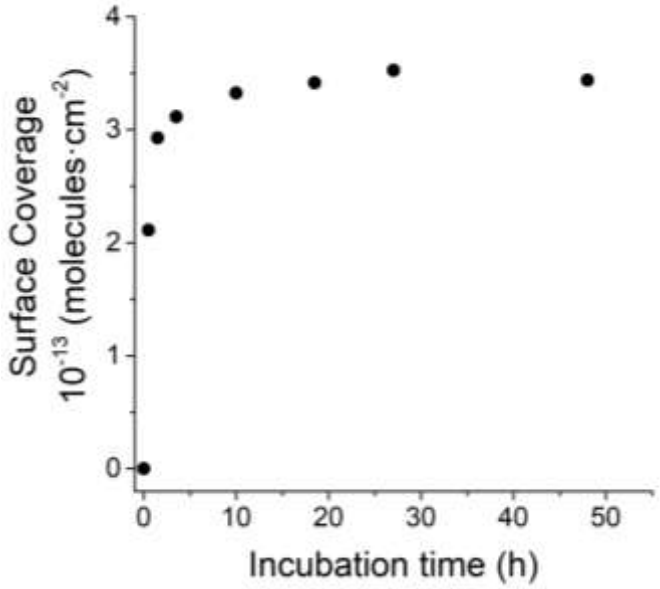

Figure S3. Surface coverage vs. time for a QCM resonator incubated in a 10^{-6} M solution of {**[1]:CB[7]**}$[Cl]_2$

S3. {[1]:CB[7]}[Cl]$_2$ surface coverage

A bearing analysis of the AFM images was made in order to calculate the {**[1]:CB[7]**}[Cl]$_2$ surface coverage (Figure S4). In a bearing analysis, the depths of all pixels of the image with respect to a reference point, i.e., the highest pixel, are analysed to give an accurate estimation of the percentage of area covered by features, i.e. surface coverage, at every pixel depth. From the images in Figure S4 a surface coverage of 95 ± 1 % is determined

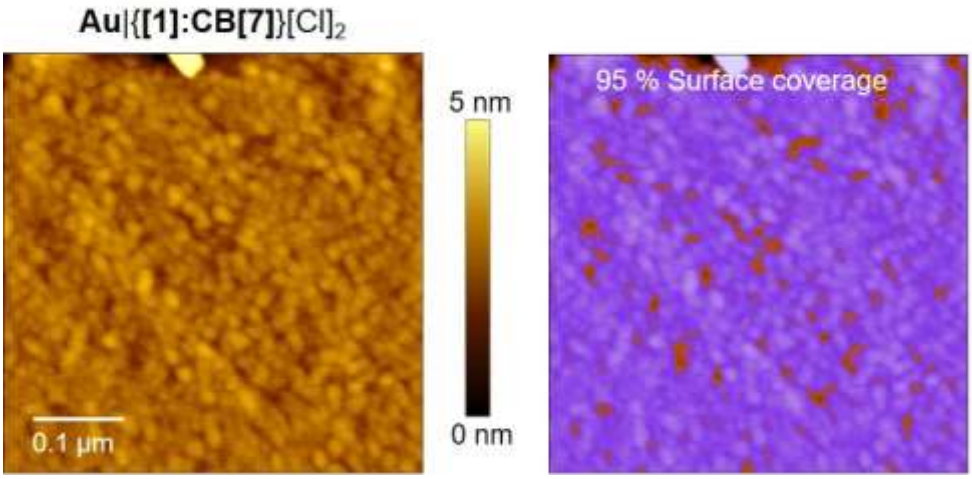

Figure S4. A 500x500 nm^2 AFM image of a {**[1]:CB[7]**}[Cl]$_2$ film without (left) and with the mask in blue revealing film-free areas (right).

S4. Thickness of a {[1]:CB[7]}[Cl]$_2$ SAM.

The thickness of {[1]:CB[7]}[Cl]2 SAM on the gold substrates was estimated using the attenuation of the Au4*f* signal according to: $I_{SAM} = I_{substrate} \exp(-d/\lambda \sin \theta)$, where d is the film thickness, I_{SAM} and $I_{substrate}$ are the average of the intensities of the Au4*f* 5/2 and Au4*f* 7/2 peaks attenuated by the SAM and from clean gold, respectively, θ is the photoelectron take-off angle, and λ = 4.2 ± 0.1 nm,[5] is the effective attenuation length of the photoelectron (Figure S4). A thickness value of (1.50 ± 0.04) nm was obtained, in agreement with the formation of a monolayer of {**[1]:CB[7]**}[Cl]$_2$ as the molecular length of **1** is 1.95 nm as determined by Spartan´08.

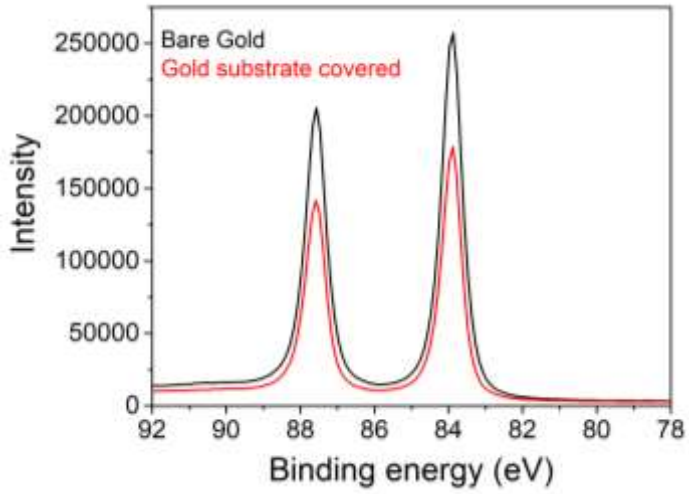

S5. Incorporation of gold nanoparticles (AuNPs)

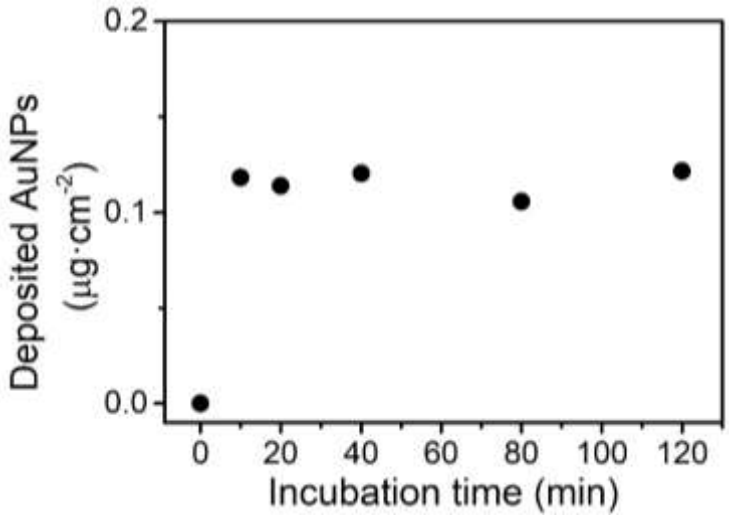

Figure S6. Surface density of gold nanoparticles as deposited onto a {**[1]:CB[7]**}$[Cl]_2$ film immersed in a dispersion of AuNPs vs. the incubation time.

Diameter and height of the AuNPs

Diameters and heights of AuNPs were obtained by using height profiles across an AFM image as shown in Figure 2b over more than 200 individual particles. The statistical analysis of the data extracted from AFM image allows us to conclude that these AuNPs exhibit an average diameter of 5.5 ± 2 nm (corrected by the tip convolution[6]) and an average height of 4.1 ± 2 nm. Histograms showing the diameter and height value distributions are depicted in Figure S7.

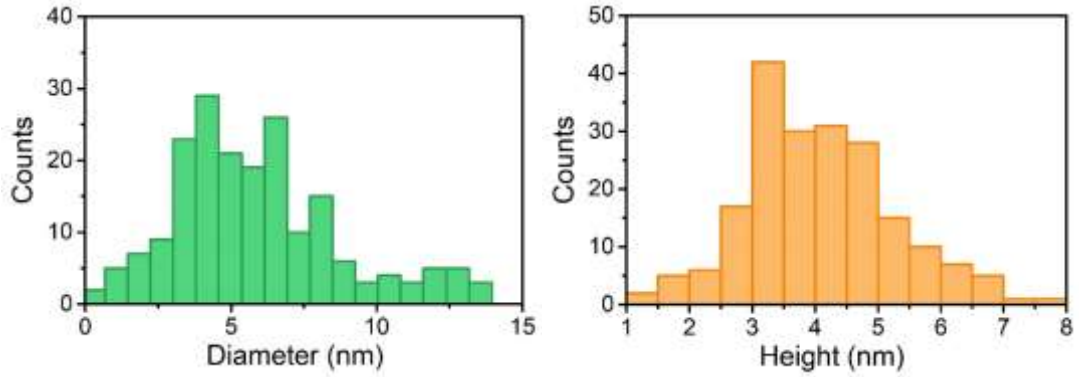

Figure S7. Histograms showing the particle diameter (corrected by the tip convolution), and height distributions, corresponding to over more than 200 individual particles.

Incorporation of AuNPs onto a [1]$[Cl]_2$ **film**

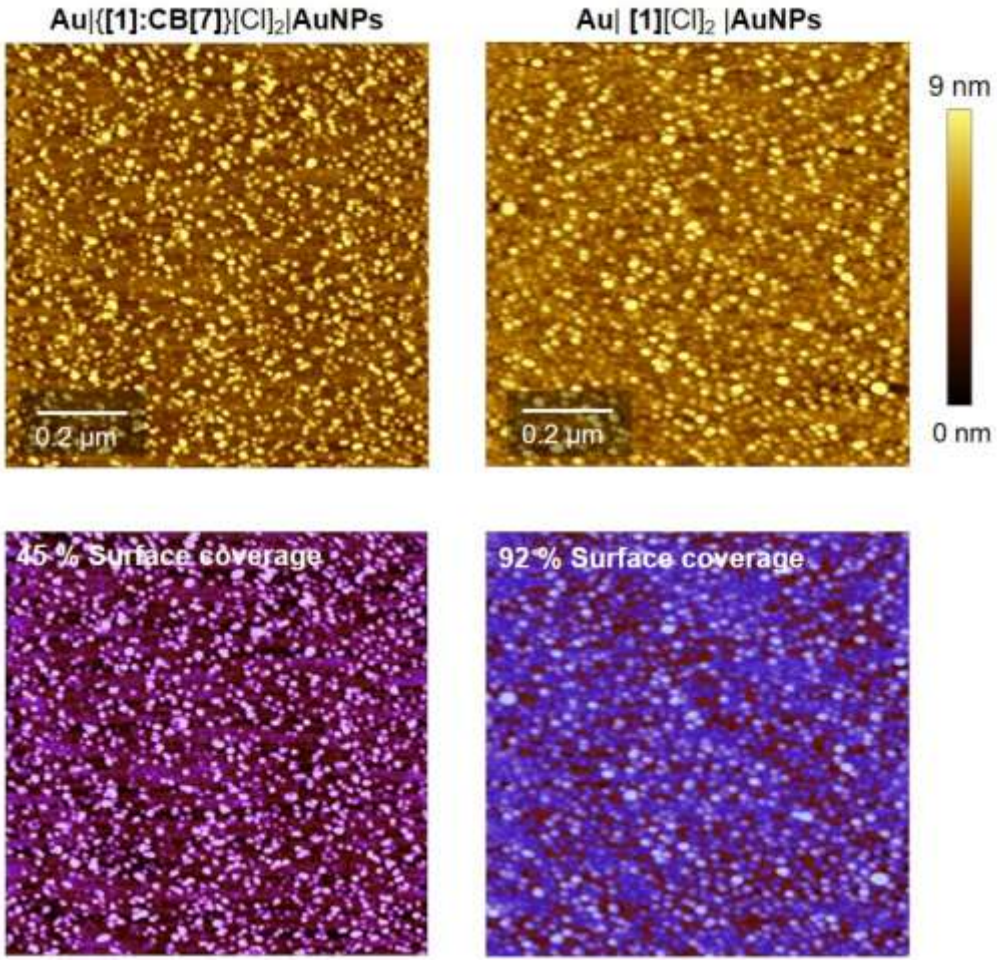

Figure S8. (top) AFM images of a SAM of {**[1]:CB[7]**}$[Cl]_2$ (left) and **[1]**$[Cl]_2$ (right) after incubation in a dispersion of AuNPs. (bottom) Same AFM images with the color mask unveiling AuNPs-free areas.

S6. I-V curves

For the **Au**|{**[1]:CB[7]**}$[Cl]_2$|**AuNP** structure

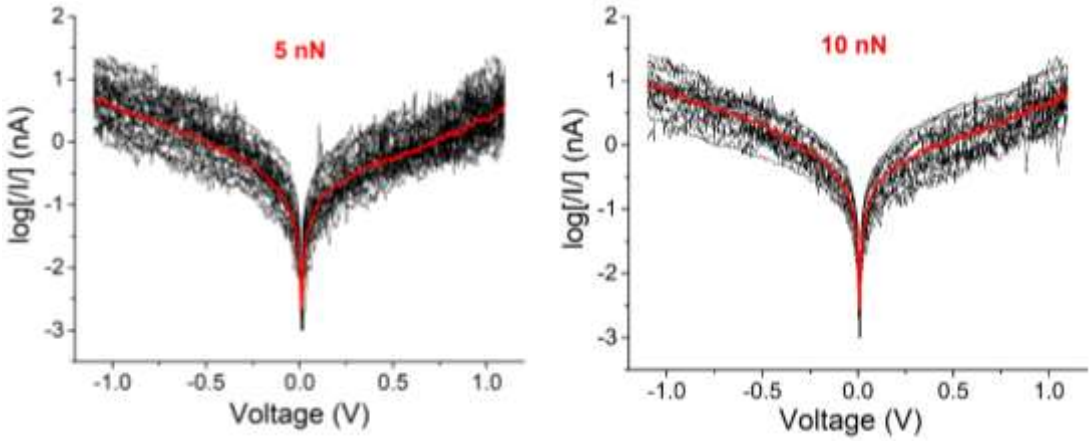

Figure S9. Log[|*I*|] versus voltage (ca. 250 curves) measured at a set point force of 5 and 10 nN. Averaged curves as shown as the red line.

For the **Au**|**1**$[Cl]_2$|**AuNP** structure

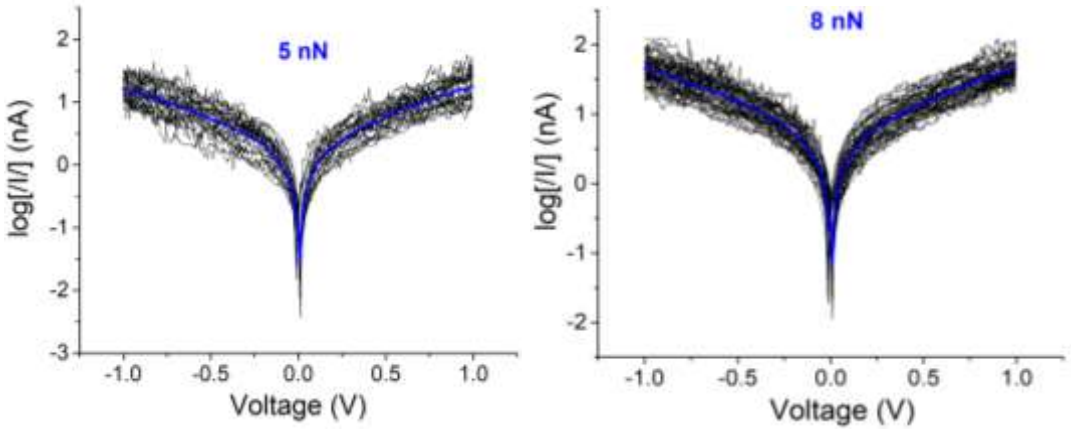

Figure S10. Log[|*I*|] versus voltage (ca. 120 curves) measured at a set point force of 5 and 8 nN. Averaged curves as shown as the blue line.

For the **Au**|**1**[Cl]$_2$|**AuNP** structure

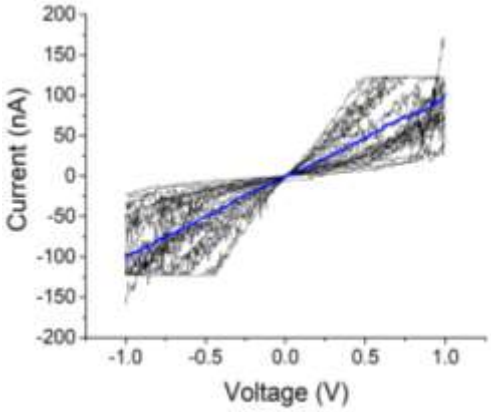

Figure S11. *I-V* curves (ca. 75 curves) measured at a set point force of 12 nN. Averaged curve is shown as the blue line. As the conductance increases substantially at this set point force, the current saturates at +/- 120 nA, limited by the current amplifier employed.

S7. Conductance *vs*. set-point force

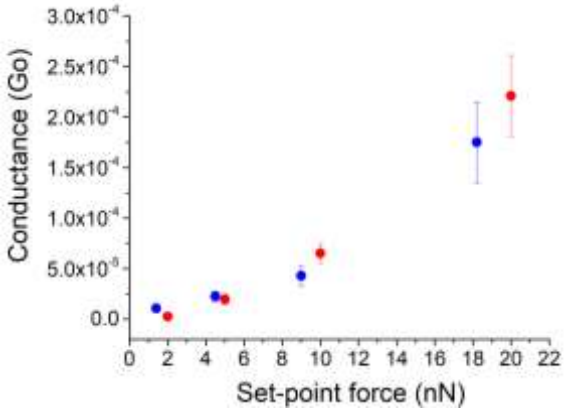

Figure S12. Conductance values versus the applied set point-force determined by locating the tip of the c-AFM onto a gold nanoparticle (red symbols) or directly above the film, free AuNPs areas in Figure 2b (blue symbols), for an **Au**|{**[1]:CB[7]**}[Cl]$_2$|**AuNP** structure.

S8. References

1. Fathalla, M.; Strutt, N. L.; Barnes, J. C.; Stern, C. L.; Ke, C. F.; Stoddart, J. F., Fluorescence Enhancement of a Porphyrin-Viologen Dyad by Pseudorotaxane Formation with Cucurbit[] Uril. *Eur. J. Org. Chem.* **2014**, *2014*, 2873-2877.
2. Freitag, M.; Gundlach, L.; Piotrowiak, P.; Galoppini, E., Fluorescence Enhancement of Di-P-Tolyl Viologen by Complexation in Cucurbit[7]Uril. *J. Am. Chem. Soc.* **2012**, *134*, 3358-3366.

3. Claveria-Gimeno, R.; Velazquez-Campoy, A.; Pey, A. L., Thermodynamics of Cooperative Binding of Fad to Human Nqo1: Implications to Understanding Cofactor-Dependent Function and Stability of the Flavoproteome. *Arch. Biochem. Biophys.* **2017**, *636*, 17-27.
4. Sauerbrey, G., Verwendung Von Schwingquarzen Zur Wagung Dunner Schichten Und Zur Mikrowagung. *Z. Phys.* **1959**, *155*, 206-222.
5. Bain, C. D.; Whitesides, G. M., Attenuation Lengths of Photoelectrons in Hydrocarbon Films. *J. Phys. Chem.* **1989**, *93*, 1670-1673.
6. Canet-Ferrer, J.; Coronado, E.; Forment-Aliaga, A.; Pinilla-Cienfuegos, E., Correction of the Tip Convolution Effects in the Imaging of Nanostructures Studied through Scanning Force Microscopy. *Nanotechnology* **2014**, *25*, 395703.